Cavity-Coupled Plasmonic Device with Enhanced Sensitivity and Figure-of-Merit

Mohsen Bahramipanah,* Shourya Dutta-Gupta, Banafsheh Abasahl, and Olivier J. F. Martin

Nanophotonics and Metrology Laboratory (NAM), Swiss Federal Institute of Technology Lausanne (EPFL), 1015 Lausanne, Switzerland

ABSTRACT Using full-wafer processing, we demonstrate a sophisticated nanotechnology for the realization of an ultrahigh sensitive cavity-coupled plasmonic device that combines the advantages of Fabry–Perot microcavities with those of metallic nanostructures. Coupling the plasmonic nanostructures to a Fabry–Perot microcavity creates compound modes, which have the characteristics of both Fabry–Perot and localized surface plasmon resonance (LSPR) modes, boosting the sensitivity and figure-of-merit of the structure. The significant trait of the proposed device is that the sample to be measured is located in the substrate region and is probed by the compound modes. It is demonstrated that the sensitivity of the compound modes is much higher than that of LSPR of plasmonic nanostructures or the pure Fabry–Perot modes of the optical microcavity. The response of the device is also investigated numerically and the agreement between measurements and calculations is excellent. The key features of the device introduced in this work are applicable for the realization of ultrahigh sensitive plasmonic devices for biosensing, optoelectronics, and related technologies.

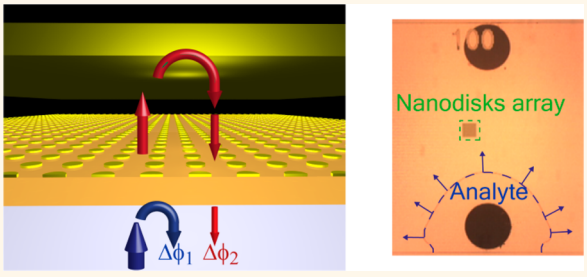

KEYWORDS: plasmon · Fabry–Perot · nanoantennas · sensor · FDTD

Recent developments in nanotechnology have led to the realization of new optical sensors that can measure a broad range of analytes in both liquid and gaseous forms.[1−10] Sensors based on surface plasmon resonances have attracted significant attention for chemical and biological sensing applications, thanks to their ability to confine light at the nanoscale well below the diffraction limit, which provides record sensitivity and low noise.[11] Plasmons supported by thin films (excited *via* Otto or Kretschmann configuration),[12−17] plasmonic resonators,[18] nanocavities,[19,20] nanoparticles,[21−26] nanocluster,[27] nanopillars,[28] nanoantennas,[29] and nanorods[30] are some of the numerous configurations for plasmonic sensors which have been suggested to take advantage of the field localization in the subwavelength sensing region. All these devices are designed to enhance the refractive index sensitivity, which is defined as the ratio of the shift in resonance wavelength to the change in the refractive index of the analyte.[31] The refractive index sensitivity depends on the characteristics of the fields in the active regions of plasmonic nanostructures and the perturbations of the fields caused by the interactions of the analytes within those regions.[32] However, localized surface plasmon resonance (LSPR) sensors are characteristically insensitive to changes happening outside the active region of the structure, and their spatial sensing depth is accordingly constrained to a few nanometers around the nanostructure.[33−35] Furthermore, the overall figure-of-merit (FoM), which is defined as the refractive index sensitivity divided by plasmon resonance line width,[31] of the LSPR-based sensors harshly suffers from the large plasmon resonance line width associated with the large intrinsic absorption of metals at optical wavelengths.[36−42]

To increase the FoM, significant research efforts have been devoted to boosting the sensitivity of metallic nanostructures by optimizing their shape.[38,43−45] Moreover, several designs including plasmon hybridization,[46] transformation optics,[47] and subgroup decomposition,[48] have been suggested to narrow the resonance line width of plasmonic nanostructures. However, the spectral line width of these resonances is still considerably larger than those of propagating surface plasmons.[14,31,49,50]

The most notable way of narrowing the line width is to couple the broad plasmon

* Address correspondence to mohsen.bahramipanah@epfl.ch.

Received for review May 17, 2015 and accepted July 1, 2015.

Published online July 01, 2015
10.1021/acsnano.5b02977

resonance of plasmonic nanostructures to a narrow resonance system. It has been shown in the plasmonic analogue of electromagnetically induced transparency that coupling a broad plasmon super-radiant mode to a narrow subradiant one leads to excitation of a sharp Fano line shape resonance.[21,27,51−58] The resulting resonance has superior refractive index sensing properties thanks to the control of the radiative losses, compared to Lorentz-resonant systems.[56] Additionally, compound modes generated because of the interaction between localized and propagating plasmons in a periodic gold grating array placed close to a thin gold film have also been investigated recently.[59−62] These resonances exhibit both characteristics of localized and propagating surface plasmons, which lead to a high sensitivity to the refractive index variations.

Alternatively, plasmon resonances can also be coupled to an optical microcavity to decrease the resonance line width.[63−68] The line width of such a cavity-coupled plasmon resonance is determined by the cavity quality factor which modifies the radiative damping. The general characteristic of cavity-coupled plasmonic sensors that have been reported so far is that the sensing medium is localized outside the cavity and is probed by the localized field of the plasmonic structure. Therefore, the dielectric microcavity just contributes to narrowing the line width of the cavity-coupled plasmonic system and does not play a crucial role for sensing. To the best of our knowledge, the only work on a cavity-coupled plasmonic structure that benefitted from the cavity modes for sensing was the nanosensor platform proposed by Schmidt *et al.*[68] They showed that the optical characteristics of the substrate on a nanoscale area could be modified by photobleaching the cavity layer using ultraviolet light, thereby changing its refractive index. However, as the material of the substrate cannot be changed once it has been fabricated, the applications of this cavity-coupled plasmonic sensor are severely limited and in its present form it cannot be applied for sensing analytes in liquid.

In this paper, we demonstrate that the coupling of the dipolar plasmon resonance of a two-dimensional nanodisks array to the narrow resonances of an optical Fabry−Perot microcavity creates compound modes, boosting both the sensitivity and FoM. It is shown that this cavity−coupled plasmonic system excellently combines the advantages of Fabry−Perot microcavities with those of plasmonic nanostructures, providing exceptional features such as ultrahigh sensitivity and FoM, large spatial sensing depth, and a strongly improved detection resolution. In particular, we study the case where the cavity-coupled plasmonic device is fabricated with the sensing medium inside the substrate region of the structure. We reveal the optical properties of this device using bright-field optical microscopy and give a detailed explanation of the underlying physics using finite-difference time-domain (FDTD) simulations. Finally, we discuss the sensing properties of this structure and demonstrate them experimentally. Let us emphasize that such a cavity-coupled plasmonic device benefits both from the LSP resonance and Fabry−Perot modes, for which respective contributions can be distinguished in the optical response of the compound modes. Furthermore, having the sensing medium inside the substrate region makes possible the joint utilization of both the LSP and the Fabry−Perot resonances for sensing the refractive index variations.

RESULTS AND DISCUSSION

Cavity-Coupled Plasmonic Structure. In the optical system investigated here, the localized surface plasmon resonance is supported by the subwavelength metallic nanodisks. Their resonance wavelength can be tuned by changing the size of the nanodisks, the background, or the metal. One of the major limitations of using such a LSPR structure as a refractive index sensor is its large line width, which is caused by the large intrinsic losses of metals. Alternatively, Fabry−Perot cavities have narrow line widths which are more suitable for sensing applications;[69−76] however, their field localization is very poor. Thus, we propose here to effectively reduce the line width while maintaining the field localization by coupling the plasmonic structure to an optical microcavity.

The cavity-coupled plasmonic structure studied here is shown in Figure 1a. It consists of two functional layers: the top layer with a two-dimensional gold nanodisks array placed on top of an ITO-coated glass substrate and the bottom layer made up of a 200 nm-thick gold metallic plane deposited on a SiO_2-coated silicon substrate, which acts as a back reflector. A 200 nm-thick SiO_2 film is also deposited on top of the gold reflective film as protective layer. Parylene is used as spacer between these two functional layers to create a microcavity with desired thickness. An ITO-coated glass substrate is placed upside down on the parylene spacer to form a Fabry−Perot resonant cavity, Figure 1a.

Simulations are performed with a homemade three-dimensional FDTD code. The structure is excited by a transverse magnetic (TM) polarized Gaussian modulated (in time) pulse source centered around the frequency of interest, with a plane wave spatial distribution and a normal incidence. The plane wave propagates in the glass region along the *z*-direction with the electric field polarized along the *x*-direction, Figure 1a. To have a dominant dipolar plasmon resonance in the investigated spectral range between 600 and 1000 nm, the diameter, thickness, and period of the nanodisks array are fixed at 210, 50, and 300 nm, respectively, unless stated otherwise. Further details on the simulation method are presented in the Supporting Information.

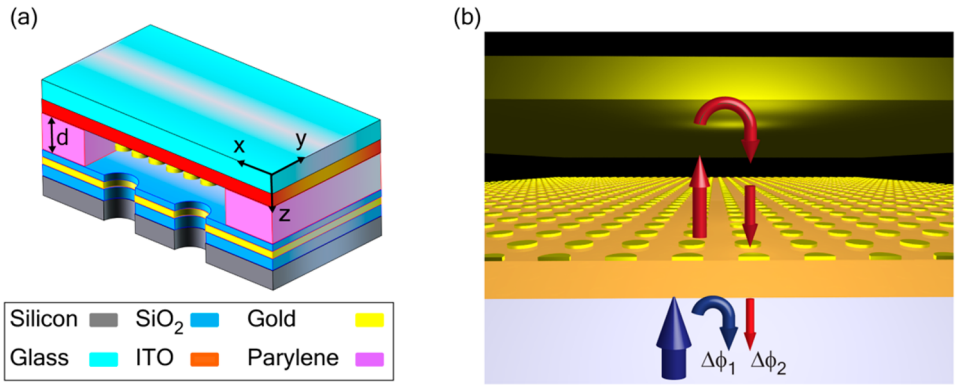

Figure 1. (a) Schematic of the cavity-coupled plasmonic structure and (b) light paths through the structure.

When the structure is illuminated from the glass side, some of the light is reflected back from the nanodisks array, with a phase change of $\Delta\phi_1$, and some of the light is transmitted into the microcavity, as illustrated in Figure 1b. During one round-trip inside the Fabry–Perot cavity, the light is partly reflected back from the nanodisks array into the cavity and partly transmitted out of the cavity with a $\Delta\phi_2$ phase change. When the geometrical parameters of the nanodisks array and Fabry–Perot cavity are properly chosen, the transmitted light from inside the cavity will have an odd multiple of π phase difference with the light reflected back from the nanodisks array; that is, $\Delta\phi_2 - \Delta\phi_1 = (2k - 1)\pi$, with k being an integer, and destructive interference for the total reflection from the structure will be achieved. In this case, a net absorption of 1 at the corresponding wavelengths can be observed, that is, perfect absorption.[77] However, when the Fabry–Perot resonances coincide with the LSPR mode of the nanodisks array, the transmitted light from the cavity will have an even multiple of π phase difference with the light reflected back from the nanodisks array; that is, $\Delta\phi_2 - \Delta\phi_1 = (2k)\pi$, and constructive interference for the total reflection will be achieved, which leads to a near unity reflection.

First, we study the effect of the cavity length on the optical response of the system. For the time being, the material inside the cavity is assumed to be air ($\varepsilon = 1$). The normalized reflectance and the phase difference between the transmitted light from the cavity and the reflected light from the nanodisks array are shown as a function of the wavelength and of the cavity length in Figure 2a,b. Figure 2a clearly shows the Fabry–Perot modes and their mode number N. In the vicinity of these Fabry–Perot resonances, phase differences between the transmitted light from the cavity and the reflected light from the nanodisks array exhibit strong variations within its value of $\pm\pi$, Figure 2b. In this case, destructive interference for the reflection is achieved. As can be seen in Figure 2a,b, for a fixed wavelength, the higher order modes of the cavity-coupled plasmonic structure exhibit the Fabry–Perot resonance condition with increasing microcavity length. The corresponding microcavity lengths, which satisfy the condition of destructive interference for the reflected light, and the corresponding reflection efficiencies are given in Table 1 (normal font). Moreover, there is one region in Figure 2a,b where the Fabry–Perot dips vanish, such that near unity reflection is achieved. This region, highlighted by a horizontal white dashed line, corresponds to the LSPR mode. We observe that when the Fabry–Perot resonances coincide with the LSPR mode of the nanodisks array, the transmitted light from the cavity is in-phase with the reflected light from the nanodisks array and constructive interference of the reflected planewaves leads to near unity reflection. When the cavity length is varied, this interaction with the plasmon mode occurs whenever the Fabry–Perot resonance is equal to the LSPR resonance. Vertical black arrows in Figure 2a,b indicate these resonant modes. It is obvious from the phase distribution that the constructive interference condition highly depends on the cavity length. In fact, a small variation in the cavity length can jeopardize the constructive interference condition. The corresponding microcavity lengths, which lead to constructive interference for the reflection, are also depicted in Table 1 (bold font). For a meaningful comparison, the normalized reflectance as a function of the wavelength and cavity length for a conventional Fabry–Perot cavity with a 50 nm thin gold layer instead of the two-dimensional nanodisks array is shown in Supporting Information, Figure S2a. This figure exhibits the conventional Fabry–Perot resonant modes. However, since the top boundary does not support any LSPR modes due to the absence of nanostructures, the near unity reflection peak cannot be achieved, and instead we can see a dip.

Cuts through Figure 2 panels a (blue solid line) and b (red dotted line) for the cavity length of 1830 nm are shown in Figure 2c. For comparison, a cut through Figure S2a for the same cavity length of 1830 nm is also shown in Figure S2b. As can be seen in the reflection spectrum of the cavity-coupled plasmonic structure, a nearly perfect destructive interference in the reflection

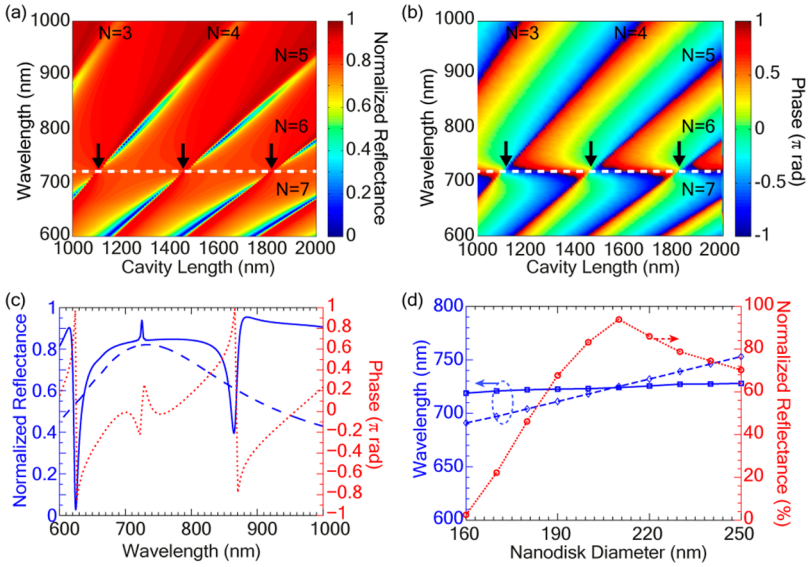

Figure 2. Colormaps of (a) normalized reflectance and (b) phase difference as a function of the wavelength and cavity length for cavity-coupled plasmonic structures shown in Figure 1. (c) Normalized reflection spectra (blue solid line) and phase difference (red dotted line) for a cavity-coupled plasmonic structure for 1830 nm cavity length. The reflection spectrum for a bare two-dimensional gold nanodisks array without the underlying Fabry–Perot cavity is also shown as blue dashed line. (d) LSPR wavelength for a bare two-dimensional nanodisks array (blue dashed line) and the normalized reflectance (red dotted line) for the second mode of the proposed cavity-coupled plasmonic structure as a function of the size of the nanodisks. For clarity, the corresponding Fabry–Perot mode, which results in constructive interference, is also shown (blue solid line). For the phase plots, the phase difference of the transmitted light outside the cavity with the reflected light from the nanodisks array are calculated and shown.

TABLE 1. Resonant Mode Number, Resonance Wavelength, and Normalized Reflectance for the Resonant Modes and Their Corresponding Microcavity Length[a]

d (nm)	resonant mode number (*N*)	resonance wavelength (nm)	normalized reflectance (%)
1100	**4**	**725**	**94.5**
1220	4	776	0.04
1280	5	652	0.3
1460	**5**	**725**	**94.2**
1600	5–6	775–652	0.1–0.3
1830	**6**	**725**	**93.9**
1930	7	651	0.4
1990	6	776	0.02

[a] Bold font and normal font indicate the constructive and destructive interference cases, respectively.

spectrum and correspondingly near unity absorption at $\lambda = 624.7$ nm can be achieved. The phase difference between the transmitted light from the cavity and the reflected light from the nanodisks array is almost π. The absorption efficiency is about 97.18% at this wavelength. On the other hand, perfect constructive interference for the reflection (phase difference of zero) and correspondingly near unity reflection, with a reflection efficiency of about 93.87%, at $\lambda = 725$ nm is also achieved. Moreover, we can see another mode at $\lambda = 864.5$ nm with an absorption efficiency of about 61.4%, for which neither perfect constructive or destructive interference occur. For comparison and qualitative analysis, the normalized reflection spectrum of a bare two-dimensional gold nanodisks array on top of the ITO-coated glass substrate, without the presence of the underlying cavity, is also shown in Figure 2c (blue dashed line), from which we can see the dipolar resonance at the wavelength of $\lambda = 725$ nm. The reflection efficiency is about 82.12% at this wavelength. Despite some minor similarities in the peak resonance wavelength, the reflection spectra for the cavity and no-cavity systems are significantly different, indicating that the cavity has an important impact on the optical response of the structure. The large line width of the dipolar resonance peak of the bare two-dimensional nanodisks array structure is 432.8 nm (full-width at half-maximum, fwhm). On the other hand, the line widths of the resonance dips and peak for the cavity-coupled plasmonic structure are 11.1 nm, 3 nm, 12.5 nm at their corresponding resonance wavelength $\lambda = 624.7$ nm (third mode), $\lambda = 725$ nm (second mode), $\lambda = 864.8$ nm (first mode), respectively. This very significant narrowing in the line width of the cavity-coupled plasmonic structure arises from the high quality factor of the microcavity and has a positive influence on the sensing capabilities of the structure, as will be shown later. For comparison, the line widths of the conventional Fabry–Perot cavity modes, shown in Supporting Information, Figure S2b, are 2.4, 3.4, and 4.7 nm, respectively; note that the second hybrid mode is slightly narrower than the corresponding mode of the conventional Fabry–Perot cavity.

Let us now consider the effect of detuning the LSPR wavelength with respect to the Fabry–Perot mode on the peak observed in the spectral response. Figure 2d

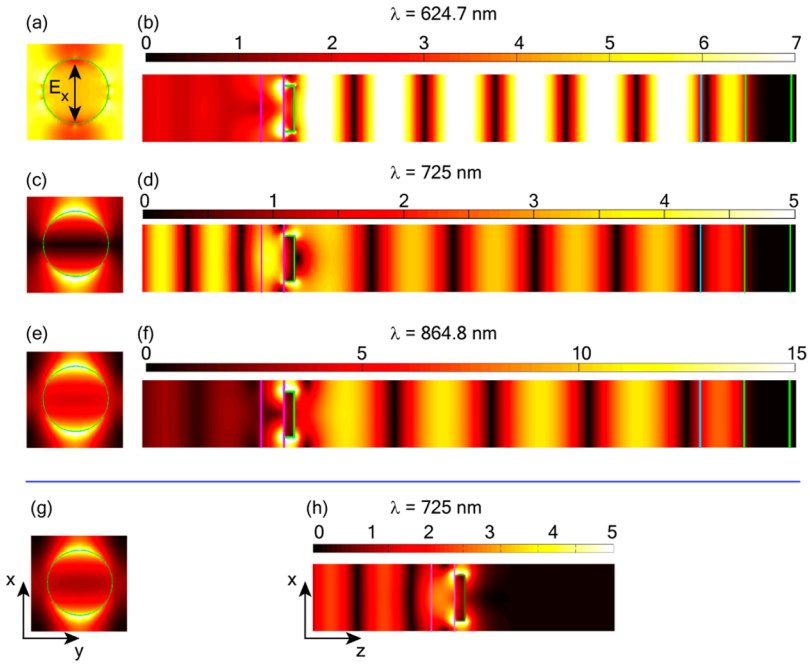

Figure 3. Total electric field amplitude distributions, at the resonance wavelengths of (a,b) $\lambda = 624.7$ nm, (c,d) $\lambda = 725$ nm, and (e,f) $\lambda = 864.8$ nm for cavity-coupled plasmonic structure and (g,h) at $\lambda = 725$ nm for the bare two-dimensional gold nanodisks array. The left panel shows the local electric field distributions in the *xy* plane and the right panel gives the electric field distributions in the *xz* plane cut through the center of the gold nanodisks.

shows the influence of the nanodisks size on the LSPR wavelength for a bare two-dimensional nanodisks array (blue dashed line) in addition to the Fabry–Perot mode (blue solid line). As the size of the nanodisks is increased from 160 to 250 nm, a red shift of the plasmon resonance is observed from 691 to 753 nm, as expected.[78] The intersection of these two lines determines the exact dimension of the nanodisks at which constructive interference can be achieved. Furthermore, the normalized reflectance of the second mode as a function of the size of the nanodisks for the complex cavity-coupled plasmonic structure is also depicted (red dotted line). A strong variation of the reflectance is clearly seen. For example, for the size of 160 nm a reflectance of 2.52% is obtained which increases to 93.87% for the nanodisks size of 210 nm. A further increase in the nanodisks size results in a decrease in the reflectance. This indicates that the peak observed in the spectrum for 210 nm is due to the constructive interference, and deviations of the LSPR from the Fabry–Perot mode result in a change in the interference condition which transforms the peak into a dip.

For better understanding of the physics behind the proposed cavity-coupled plasmonic structure, FDTD simulations of the total electric field amplitude distributions (absolute value) at the resonance wavelengths of $\lambda = 624.7$ nm, Figure 3a,b, $\lambda = 725$ nm, Figure 3c,d, and $\lambda = 864.8$ nm, Figure 3e,f are compared with the electric field amplitude distribution of the plasmon mode of the bare two-dimensional nanodisks array, Figure 3g,h. In particular, the left panel shows the local electric field distributions in the *xy* plane, 5 nm above the nanodisk inside the cavity, and the right panel illustrates the electric field distributions in the *xz* plane cut through the center of the gold nanodisks. To ease interpretation of the presented field distributions, we note that the structures are illuminated by a plane wave which is polarized in such a way as to contain only the E_x component of the electric field, black arrow in Figure 3a.

The field plots corresponding to the third mode at $\lambda = 624.7$ nm, Figures 3a,b, clearly show that the electric field is strongly enhanced not only at the edges of the nanodisk but also inside the Fabry–Perot cavity because of destructive interference. From the *xy* field distribution, Figure 3a, it is obvious that the dipolar plasmon resonance cannot be effectively exited and the Fabry–Perot component dominates in this compound mode. Furthermore, the field in the *xz* plane shows a standing wave pattern within the cavity, characteristic of a Fabry–Perot kind of resonance. From the same plot, it can be observed that the strong fields associated with the nanodisks are located primarily in the ITO layer, indicated by pink lines in Figure 3b. The absence of a strong standing wave pattern outside the structure also provides additional proof of destructive interference. In contrast to the third mode at which almost destructive interference is obtained, the second mode at $\lambda = 725$ nm exhibits constructive interference and hence completely different field distributions. Standing wave patterns can be observed both inside and outside the cavity, Figure 3d. However, the field intensities for the second mode

inside the cavity are lower as compared to the fields observed for the third mode at identical spatial locations, Figure 3b and Figure 3d. In the case of this mode, the fields associated with the nanodisks are predominantly localized in the cavity region as opposed to the ITO layer. Even though the field localizations due to the nanodisks are different for the third and the second modes, the maximum intensities observed are very similar. The *xy* field plot of the second mode, Figure 3c, clearly shows the excitation of the dipolar plasmon resonance associated with the nanodisks. This is in contrast with the fields observed on a similar plane for the third mode, Figure 3a. Therefore, in the case of the second mode, both the Fabry−Perot and LSPR modes play a crucial role for creating the compound mode. The field distributions for the first mode, $\lambda = 864.8$ nm, which exhibit neither perfect constructive or perfect destructive interference of the reflected light, are shown in Figure 3e,f. In this case the electric field is localized at both the edges of the nanodisk as well as inside the Fabry−Perot cavity. The maximum intensities observed for this mode are higher as compared to that for the other two modes. Figure 3e shows the *xy* field plot elucidating the excitation of a dipolar plasmon resonance, similar to the one associated with the second mode. Additionally, the electric field associated with the nanodisks is localized in both the cavity region as well as in the ITO layer, Figure 3f. For completeness, we also present the electric fields for nanodisks in the absence of the cavity in both the *xy* and *xz* planes, Figure 3g,h. The electric field in this case is just localized at the edges of the nanodisk. As can be seen, the field distribution of the dipolar mode matches quite well with the field distributions computed for the second mode of the cavity-coupled plasmonic structure, Figure 3c,d.

As discussed before, the second mode of the cavity-coupled plasmonic structure is much narrower than the first and third modes. The physical principle of this line narrowing can be evaluated from the loss mechanisms in play within the cavity-coupled plasmonic structure. From Figure 3b,f it is clearly seen that the light is mostly concentrated inside the cavity. Since the main source for losses in the system is the plasmonic nanostructures, the concentrated light inside the cavity would face higher losses when compared to the second mode, in which most of the light is concentrated outside the cavity, Figure 3d. Therefore, the higher rate of energy loss relative to the stored energy inside the cavity for the first and third modes results in a lower quality factor and broadening of the line widths.

The aforementioned numerical analysis demonstrates that the various interactions between the Fabry−Perot and the LSPR resonances can be used for constructing compound resonances with narrow line widths. In the subsequent sections, we detail the various steps used for realizing the cavity-coupled structures and the experimental validation of their sensitivity for bulk refractive index sensing.

Nanofabrication. To experimentally realize the proposed cavity-coupled plasmonic device, we have combined electron beam lithography with UV-lithography to fabricate metallic nanostructures and the microfluidic chamber defining the optical Fabry−Perot cavity. Although the fabrication is quite intricate, this geometry enables the sensing medium to be inside the substrate, in direct interaction with the plasmonic nanostructures. The fabrication process is illustrated in Figure 4.

First, a standard 4 in. crystalline silicon wafer (545 μm thickness, specification 100/P/SS/01−100) was cleaned in piranha solution (96% sulfuric acid, H_2SO_4, and 30% peroxide, H_2O_2) for 10 min at 100 °C to remove organic residue on the wafer surface. A continuous 500 nm SiO_2 layer was deposited using e-beam evaporation (Leybold Optics LAB 600H). Then, a 200 nm-thick layer of gold with a chromium adhesion layer of 2 nm was deposited on the SiO_2 layer; this layer acts as the mirror for the cavity-coupled plasmonic structure. A 200 nm-thick SiO_2 film was also deposited on top of the gold film, with a chromium adhesion layer of 2 nm, to facilitate the adhesion of parylene in the next step and also as a protective layer for the gold mirror, Figure 4a.

It is well-known that bonding glass to silicon wafers with polymer glue as the intermediate layer is possible, since the polymer layer is elastic and can be effectively heated above its glass transition temperature.[79] Among different polymers utilized to perform polymer bonding, parylene-C was used in this work both to form the microcavity and to perform the bonding operation. An advantage of parylene-C is that it is biocompatible and can be deposited at room temperature; furthermore, it does not require thermal annealing or baking cycles during deposition.[79] Therefore, 1830 nm parylene-C was deposited on the sample using a Comelec C-30-S parylene deposition system, Figure 4b.

A UV-lithography technique was used to create the microcavity in parylene. The batch priming of the substrate was done in a YES III, HMDS primer oven (BITA BeNeLux) for 10 s at 125 °C to enhance adhesion of the positive photoresist. Before coating the substrate with the photoresist, the dehydration baking step was performed on a hot plate for 4 min at 160 °C. This step has a substantial impact on adhesion of positive photoresist to the substrate. Then, a 5 μm thick layer of AZ9260 positive photoresist (AZ Electronic Materials) was spin-coated on the top of the parylene film using EVG150 coater and developer system for positive resist (EV Group). Soft baking of the substrate was then carried out on a hot plate at 115 °C for 4 min, followed by 8 min relaxation at 25 °C.

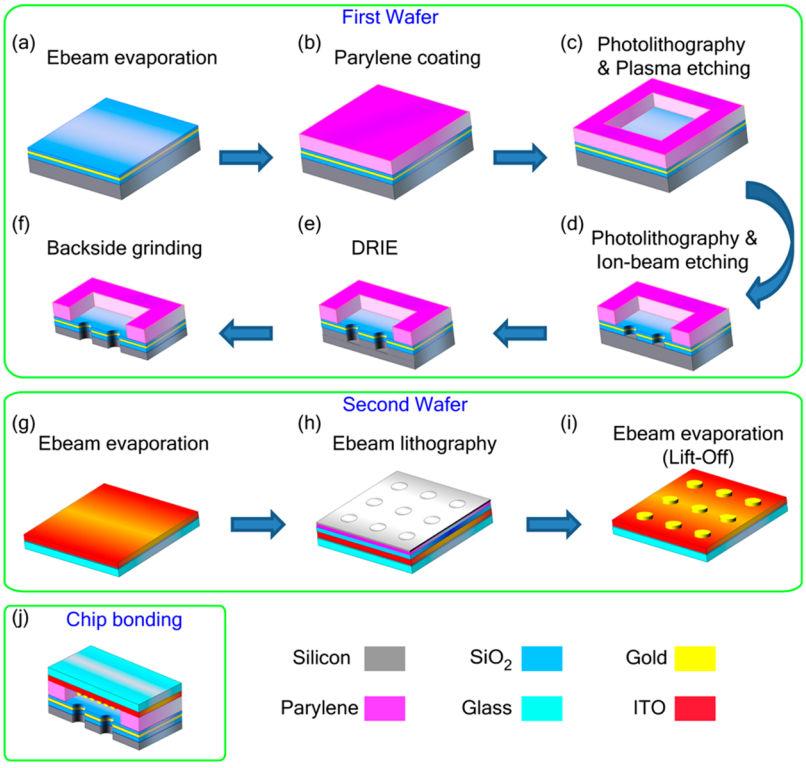

Figure 4. Process flow for the fabrication of (a–f) microcavities; (g–i) two-dimensional gold nanodisks array; (j) final chip bonding.

Then, a chrome-coated glass mask was used to transfer the patterns of the microcavities into the photoresist. The mask consists of square features (1×1 mm^2) with the pitch size of 2 mm. UV-Lithography was performed with a Karl Suss MA6 double side mask aligner (Karl Suss Inc.) in the hard contact mode between the wafer and the mask with a 10 mW/cm^2 mercury light source, and 17 s exposure time, corresponding to a dose of approximately 170 mJ/cm^2. Then the exposed areas were removed with a solvent (AZ 400 K:DI 1:4) during the development process. Using the photoresist as a mask, parylene was then successfully etched with Surface Technology Systems (STS) Multiplex ICP (RF power 800 W, platen power 150 W, O_2 flow 20 sccm, pressure 95 mTorr, time 2 min), Figure 4c. Any remaining photoresist was striped by bathing the wafer in Shipley 1165 for 10 min followed by fine rinsing with deionized (DI) water and drying with N_2 gas. The SEM image of the parylene wall of the microcavity is shown in Figure 5a. To fabricate the inlet and outlet holes inside the cavity, the wafer was spin-coated with 8 μm thick layer of AZ9260 photoresist after batch priming of the substrate in YES III, HMDS primer oven for 10s at 125 °C and a dehydration bake step for 4 min at 160 °C. After soft baking the photoresist layer at 115 °C for 4 and 20 min relaxation at 25 °C, another chrome-coated glass mask with an array of holes (200 μm in diameter) was used to transfer the patterns precisely inside the previously fabricated cavities. The exposure was performed for 24 s, corresponding to a dose of approximately

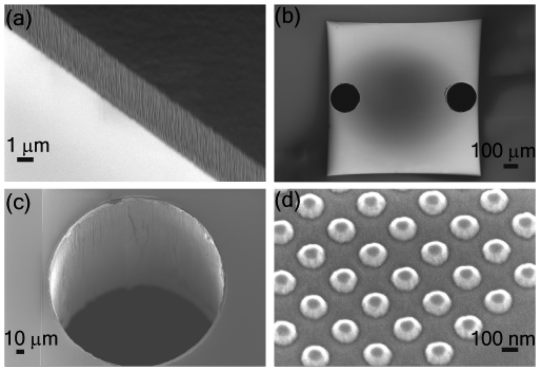

Figure 5. SEM images of the fabricated sample: (a) parylene-edge of the cavity after plasma etching; (b) cavity part of the structure with two holes as inlet and outlet; (c) microhole channel for injecting analyte inside the cavity; and (d) two-dimensional array of gold nanodisks on ITO-coated glass substrate.

240 mJ/cm^2, after precise alignment of the second mask with the previous microcavity patterns in the parylene layer. These exposures have been tuned according to the substrate material and the layers reflectivity in order to elude immoderate stress, failure in the adhesion, or undesired pattern dimensional changes. Similar to the previous step, the exposed areas were removed with a solvent (AZ 400 K:DI 1:4) during the development step by the developer. Using the patterned AZ9260 photoresist as a mask, the 200 nm SiO_2, 200 nm gold, and 500 nm SiO_2 layers were then etched by argon ions using Nexus IBE350,

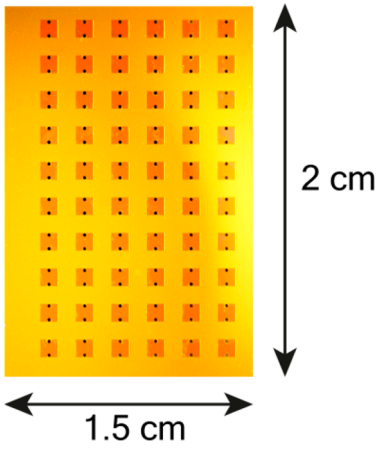

Figure 6. Photograph of the fabricated superchip containing 60 microcavities.

broad-beam ion etcher, Figure 4d. The etch rates for SiO_2 and gold were found to be 88 nm/min and 100 nm/min, respectively, for low ion damage with energy range of about 50 V. Then deep reactive ion etching (DRIE) of Si was performed, using the same AZ9260 photoresist mask, on Adixen AMS200 etcher with SF_6 plasma for 1 h with a vertical etch rate of 5 μm/min to etch 300 μm of Si wafer inside the holes, Figure 4e. The wafer was then thinned down from the backside using a DAG810 automatic surface grinder, until the paths to the holes were opened, Figure 4f. At last, any remaining photoresist was stripped by bathing the wafer in Shipley 1165 for 10 min followed by rinsing with DI water and drying with N_2 gas. The SEM image of the microcavity with the two holes inside and the magnified image of the microhole are shown in Figure 5b,c.

On the other hand, 100 nm ITO was deposited using e-beam evaporation (Leybold Optics LAB 600H) on a glass wafer (540 μm thickness), Figure 4g. Then, the two-dimensional gold nanodisks array was fabricated on the ITO-coated glass wafer using electron-beam lithography, gold evaporation, and subsequent lift-off, as shown in Figure 4h,i. The SEM image of the nanodisks array is shown in Figure 5d.

To bond these two wafers together to form the cavity-coupled plasmonic structure, the wafers were diced in 1.5 $\times$ 2 cm^2 rectangles and were then treated with O_2 plasma at 150 W during 10 s for surface activation using a Tepla 300 plasma stripper under 400 mL/min O_2 flow. Next, the wafers were bonded at 100 °C during 4 h with a pressure of 3000 mbar using Thermal Nanoimprinter EHN-3250, Figure 4j.

Figure 6 shows a photograph of the fabricated sample before the bonding process. For each chip, there are 60 microcavities with 1 $\times$ 1 mm^2 dimensions and two 200 μm circular holes in each microcavity as inlet and outlet. This wafer-scale fabrication technology yields a total number of 540 individual devices on a 4 in. wafer; each device can be used separately for different sensing applications.

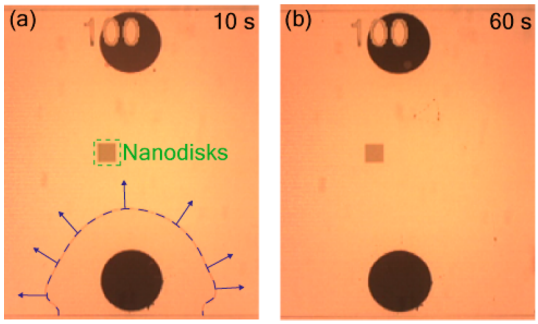

Figure 7. Microscopic images of the cavity filling with D-glucose solution after (a) 10 and (b) 60 s. The blue dashed line shows the liquid/air interface which flows from the inlet into the microcavity. The green dashed line in the middle of the structure indicates the gold nanodisks array.

The specific fabrication steps can be replaced by more low-cost fabrication techniques, such as nanoimprint lithography for the fabrication of nanostructure or injection-molding for realizing the microcavity to reduce the fabrication costs.[80,81]

Ultrahigh Sensitive Cavity-Coupled Plasmonic Biochemical Sensor. In this section, the performance of the proposed cavity-coupled plasmonic device as a biochemical sensor is evaluated. Since the reflection peak and dips, Figure 2c, of the cavity-coupled plasmonic structure are spectrally much narrower than the LSPR mode of the bare nanodisks array, they are employed to probe bulk refractive index changes with a very high resolution. The interaction of the analyte with the compound modes of the device changes the effective index of the modes, and thus the resonance wavelengths of the structure and the detection can be made by monitoring the shift in the reflection peak/dips wavelengths.

In the realized device, the microcavity can be filled *via* standard microfluidic pumps or *via* mere capillary forces. For the current study, we use the latter technique for filling the cavity. Putting a drop of analyte on top of one hole results in a self-filling procedure *via* capillary forces only, which ensures a bubble-free filling for the microcavity. The filling process is demonstrated in Figure 7 to illustrate the temporal development of the filling. In particular, this figure shows the snapshots of the cavity as visualized under a microscope at two different time points (10 s and 60 s) after the addition of the drop. No additional external pressure was introduced to the inlet. For the case of 10 s, the liquid/air interface is clearly visible (indicated by the dashed blue line). Driven by capillary forces, the solution automatically flows from the inlet into the microcavity and within 60 s the whole cavity is filled with the sensing solution without trapping any visible air bubbles. Filling *via* capillary forces is handy for simple and rapid tests of analytes and does not require any extraneous microfluidic equipment. However, since the proposed device is microfluidic compatible, it can always be

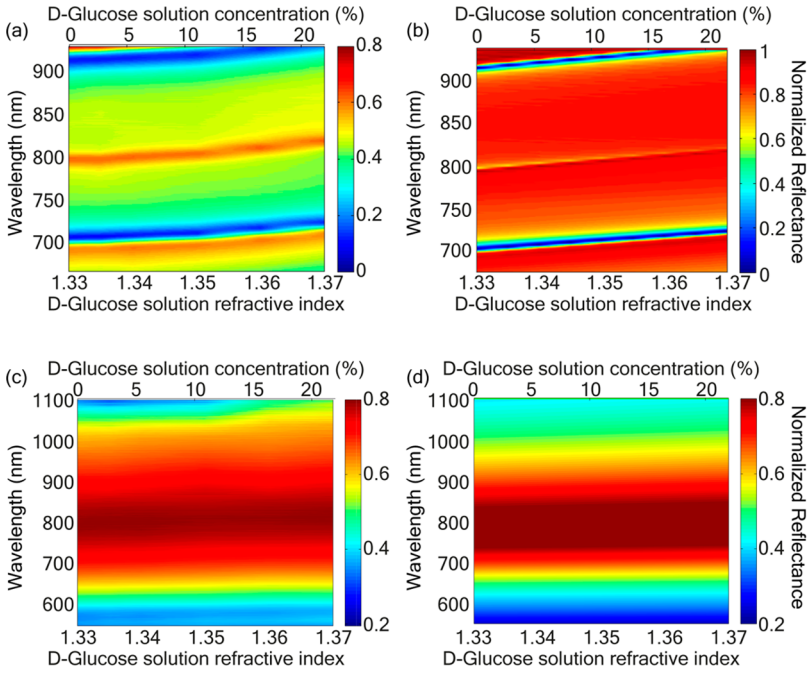

Figure 8. Colormap of the reflection spectra as a function of the wavelength and D-glucose solution refractive index; the corresponding solution concentration is also indicated. (a) Measurements and (b) numerical simulation results for the cavity-coupled plasmonic structure. (c) Measurements and (d) numerical simulation results for a bare two-dimensional gold nanodisks array.

coupled either to needles or pumps and valves to develop more sophisticated assays. Note that microfluidics also enables real-time handling of analytes.

Let us now perform bulk biochemical sensing experiments to demonstrate the sensing capability of the device. Deionized (DI) water is injected through the inlet and the reflection spectrum is measured. Subsequently, D-glucose ($C_6H_{12}O_6$) solutions with different concentrations are injected through the inlet, and the shifts of the modes are measured with respect to the wavelengths of the modes for DI water. After each sensing step, the cavity is completely washed with DI water and isopropyl alochol followed by drying with N_2 gas to make sure that no residue of glucose is left inside the cavity or on the nanostructures and that the sensor response is back to that of the DI water. The experimentally measured reflection spectra as a function of the wavelength and concentration and corresponding refractive index of the D-glucose solution are shown in Figure 8a. For comparison, we also perform bulk biochemical sensing simulations. It is assumed that the cavity is filled with D-glucose solutions in DI water with mass concentrations of 0−22%. A sensing analysis is then simulated as a uniform medium whose refractive index is changed from its original refractive index 1.33 up to 1.37 ($\Delta n = 4 \times 10^{-2}$).[82] The simulated reflection spectra as a function of the wavelength and concentration and corresponding refractive index of the D-glucose solution are illustrated in Figure 8b. As can be seen, the simulation results agree well with the experimental data. On the basis of the measurement results, the resonance wavelengths of the compound modes redshift almost linearly from 912 to 932.3 nm for the first mode, from 797.4 to 819.3 nm for the second mode, and from 707.4 to 724.9 nm for the third mode when the D-glucose solution concentration varies from 0 to 22% with a corresponding variation of its refractive index from 1.33 to 1.37.

The experimentally derived detection sensitivities, defined as the derivative of the peak wavelength versus the refractive index of the analyte, are 507.5 nm/RIU, 547.5 nm/RIU, and 437.5 nm/RIU for the first, second, and third mode, respectively. By utilizing a commercial high-performance optical spectrum analyzer (Agilent 86146B) with 10 pm wavelength resolution, the minimum detection limit for bulk sensing is as low as 1.970×10^{-5} RIU, 1.826×10^{-5} RIU, and 2.285×10^{-5} RIU for the first, second, and third modes, respectively. The sensitivity of the first mode is higher than the sensitivity of the third mode which is related to the spectral position of the resonance. Indeed, when the resonance wavelength is shifted to the red, a higher sensitivity can be achieved upon index changes. This is so because a larger fraction of the spatial region with enhanced electric fields is exposed to the material under sensing.[83] On the other hand, the sensitivity of the second mode is higher than those of the first and the third modes, since this resonance is caused by the constructive interference, i.e. the Fabry−Perot mode coincides with the LSPR mode of the nanodisks array and we can benefit from both the characteristics of Fabry−Perot mode of the

cavity and the LSPR mode of the nanostructures. However, this is a bit counterintuitive since, at the wavelength where we obtain constructive interference (second mode), the net field enhancement is lower as compared to the two other modes, Figure 3. Therefore, we would naturally expect the first and the third modes to exhibit a higher sensitivity, which is clearly not the case. A possible origin of this anomalous higher sensitivity of the second mode as compared to the other two modes could be related to the actual field distributions supported by the structure. Specifically, in case of the second mode, the majority of the fields associated with the nanodisks are contained into the cavity, with the sensing medium, whereas, in the cases of the first and the third modes, the reverse holds true; that is, the fields are mainly contained in the ITO and the substrate. Hence, higher sensitivity can be achieved for the second mode compared with the two other modes in which the Fabry–Perot resonances are dominant.

The experimentally measured fwhm of the resonant modes are 23.4, 9.3, and 19.8 nm for the first, second, and third mode, respectively, Figure 8a. Hence, our system shows a remarkably high FoM, with values of 21.68, 58.87, and 22.09 for the first, second, and third modes, respectively. The high FoM of 58.87 of the realized device greatly exceeds those of the plasmonic sensors in the case of a semi-infinite substrate, where typical FoM values are 0.6–17 for LSPR sensors without the occurrence of Fano resonance, and 2.9–21 for LSPR sensors with Fano resonance. Moreover, it is much higher than those of the SPP sensors without the occurrence of Fano resonance, in which the typical FoM values are as high as 31. However, it is almost lower than those of SPP sensors with Fano resonance, in which the typical FoM values are 48–252. A detailed summary of the resonance wavelengths, FWHMs, refractive index sensitivities, and FoM values of different plasmonic metal nanostructures along with the references are provided in Tables S1 of the Supporting Information. As expected, the smallest line width, corresponding to the largest FoM, is achieved in the constructive interference region. Hence, this cavity-coupled plasmonic device is especially well suited for boosting the sensing performances of localized plasmonic systems.

For quantitative comparison and to demonstrate the improved sensitivity with the proposed cavity-coupled plasmonic structure, the experimental and simulated reflection spectra for a bare two-dimensional array of gold nanodisks without the underlying cavity are shown in Figure 8c,d as a function of wavelength and D-glucose concentration, as well as the corresponding refractive index. We can see a good agreement between the simulation results and the experimental data. The LSPR peak wavelength redshifts almost linearly from 801 to 809 nm, when the D-glucose solution concentration varies from 0 to 22.0%, corresponding to a variation of its refractive index from 1.33 to 1.37. Based on the measurement results, the experimental detection sensitivity is calculated to be 200 nm/RIU which is almost 2.7 times lower than that for the second mode of the cavity-coupled plasmonic structure. Moreover, the fwhm of the reflection peak is 498 nm, which is much larger than those for the cavity-coupled plasmonic structure. Hence, the FoM of the bare two-dimensional nanodisks array structure is calculated to be 0.4 which is almost 147 times lower than that of the cavity-coupled plasmonic sensor.

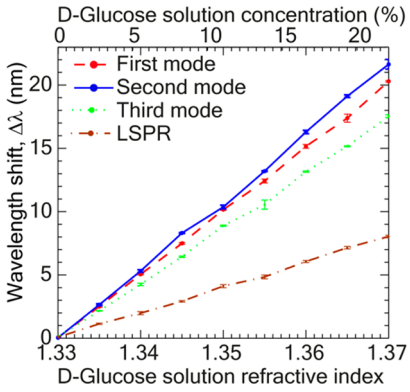

Figure 9. Experimental results for the shift in the resonance wavelengths as a function of the D-glucose solution refractive index for the cavity-coupled plasmonic structure and a bare two-dimensional nanodisks array.

In Figure 9, we summarize the measurement results for the reflection peak/dips wavelengths of the proposed cavity-coupled plasmonic device as a function of the concentration and the corresponding D-glucose solution refractive index; these data are also compared with those of the bare nanodisks array. Linear relationships can be seen between the resonance wavelengths and the D-glucose solution concentration. Moreover, larger shifts are achieved for the compound modes of the cavity-coupled plasmonic device and the highest sensitivity corresponds to the second mode, which represents the constructive interference region where the LSPR mode coincides with the Fabry–Perot mode of the cavity.

The cavity-coupled plasmonic structure has a higher refractive index sensitivity than the conventional Fabry–Perot cavity. Supporting Information, Figure S3 shows the resonance wavelength shift for the first, second, and third modes of the conventional Fabry–Perot cavity as a function of D-glucose concentration and corresponding refractive index. The shifts are 19.4, 17, and 15 nm for the conventional Fabry–Perot cavity, while they are 20.3, 21.9, and 17.5 nm for the cavity-coupled structure, leading to a significant sensitivity improvement, up to almost 30%, for the cavity-coupled structure.

Moreover, we have mentioned that an interesting feature of the proposed structure is that the analyte is in the substrate region in direct contact with the

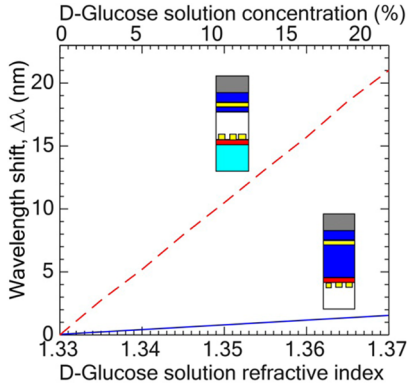

Figure 10. Resonance wavelength shifts as a function of D-glucose refractive index for the proposed cavity-coupled plasmonic structure with the sensing medium (white area) inside the cavity (red dashed line) and for the cavity-coupled plasmonic structure with the sensing medium outside the cavity (blue solid line).

plasmonic nanostructures, as opposed to other cavity-coupled plasmonic systems, where the sensing medium is outside the cavity.[64] Here, we compare these two configurations and focus on the constructive interference region in which near unity reflection and highest sensitivity can be achieved. Figure 10 shows the simulated resonant peak wavelength shifts as a function of the D-glucose solution refractive index for both geometries. In the case of the nanodisks outside the cavity, it is assumed that the cavity is filled with SiO_2. Since the Fabry–Perot mode redshifts in the presence of a SiO_2, the size of the nanodisks must be adjusted to 250 nm in order to have constructive interference. For this configuration, the shift of the resonance wavelength for a 22% D-glucose concentration is only about 1.5 nm, blue solid line in Figure 10, while for the previously discussed configuration with the analyte inside the cavity, the shift is about 21 nm which is about 14 times larger, red dashed line in Figure 10. This small shift of 1.5 nm in the resonance wavelength of the cavity-coupled plasmonic structure with the sensing medium outside the cavity, even in comparison to the bare two-dimensional array of gold nanodisks array, is also observed in previous researches on cavity-coupled plasmonic structures.[64]

CONCLUSIONS

We have introduced a novel approach to realize an ultrahigh sensitive cavity-coupled plasmonic device, using full-wafer level processing, which combines the advantages of Fabry–Perot microcavities with those of plasmonic nanostructures to boost the sensitivity and figure-of-merit. Detailed characteristics of the device are studied by FDTD numerical simulations to demonstrate the feasibility of this concept. The role played by the compound resonances arising from the constructive and destructive interferences has been discussed in detail. The experimental results demonstrate that the resonant compound mode of the device has a sensitivity of 547.5 nm/RIU, a resolution of 1.826×10^{-5} RIU, a fwhm of 9.3 nm, and a FoM of 58.87 at an optical wavelength of around 800 nm. The special feature of the proposed device is that the sample to be measured is localized in the substrate region and is probed by the compound modes. Another distinct advantage is the convenient self-filling of the microcavity employing only capillary forces, without needing any additional microfluidic structures. Furthermore, the proposed cavity-coupled plasmonic device technology is particularly promising for biomedical and biochemical applications. This combination sets groundwork for developing hybrid sensors that can be fully integrated into lab-on-chip solutions.

METHODS

Reflection Measurement. The normal incidence reflection measurements were performed using an inverted optical microscope (Olympus IX-71) coupled to a spectrometer (Jobin Yvon Horiba Triax 550). The sample was illuminated using a halogen light source focused onto the sample using a 10× objective (NA 0.25). The reflected light was collected using the same objective and analyzed using a spectrometer. The reflected intensity was normalized to the reflection from a silver mirror.

Conflict of Interest: The authors declare no competing financial interest.

Acknowledgment. It is a pleasure to acknowledge Dr. C. Santschi and Dr. C. Hibert for their support with the fabrication of the cavity-coupled plasmonic devices. This work was supported by the Swiss National Science Foundation (project CR23I2_147279).

Supporting Information Available: A detailed description of the numerical method; additional figures explaining the reflection spectrum and the sensitivity of a conventional Fabry–Perot cavity; summary of the resonance wavelengths, FWHMs, refractive index sensitivities, and FoM values of plasmonic metal nanostructures for different types of resonances along with all the references. The Supporting Information is available free of charge on the ACS Publications website at DOI: 10.1021/acsnano.5b02977.

REFERENCES AND NOTES

1. Kang, C.; Weiss, S. M. Photonic Crystal with Multiple-Hole Defect for Sensor Applications. *Opt. Express* **2008**, *16*, 18188–18193.
2. Vincenti, M. A.; Trevisi, S.; De Sario, M.; Petruzzelli, V.; D'Orazio, A.; Prudenzano, F.; Cioffi, N.; de Ceglia, D.; Scalora, M. Theoretical Analysis of a Palladium-Based One-Dimensional Metallo-Dielectric Photonic Band Gap Structure for Applications to H_2 Sensors. *J. Appl. Phys.* **2008**, *103*, 064507.
3. Lahiri, B.; Khokhar, A. Z.; De La Rue, R. M.; McMeekin, S. G.; Johnson, N. P. Asymmetric Split Ring Resonators for Optical Sensing of Organic Materials. *Opt. Express* **2009**, *17*, 1107–1115.
4. Claes, T.; Molera, J. G.; De Vos, K.; Schachtb, E.; Baets, R.; Bienstman, P. Label-Free Biosensing With a Slot-Waveguide-Based Ring Resonator in Silicon on Insulator. *IEEE Photonics J.* **2009**, *1*, 197–204.
5. Schartner, E. P.; Ebendorff-Heidepriem, H.; Warren-Smith, S. C.; White, R. T.; Monro, T. M. Driving Down the Detection

Limit in Microstructured Fiber-Based Chemical Dip Sensors. *Sensors* **2011**, *11*, 2961–2971.
6. Suárez, G.; Santschi, C.; Plateel, G.; Martin, O. J. F.; Riediker, M. Absorbance Enhancement in Microplate Wells for Improved-Sensitivity Biosensors. *Biosens. Bioelectron.* **2014**, *56*, 198–203.
7. Jalkanen, T.; Torres-Costa, V.; Makila, E.; Kaasalainen, M.; Koda, R.; Sakka, T.; Ogata, Y. H.; Salonen, J. Selective Optical Response of Hydrolytically Stable Stratified Si Rugate Mirrors to Liquid Infiltration. *ACS Appl. Mater. Interfaces* **2014**, *6*, 2884–2892.
8. Kangwen, L.; Xunpeng, M.; Zuyin, Z.; Jiakun, S.; Yun, X.; Guofeng, S. Sensitive Refractive Index Sensing with Tunable Sensing Range and Good Operation Angle-Polarization-Tolerance using Graphene Concentric Ring Arrays. *J. Phys. D: Appl. Phys.* **2014**, *47*, 405101.
9. Bonnot, K.; Cuesta-Soto, F.; Rodrigo, M.; Varriale, A.; Sanchez, N.; D'Auria, S.; Spitzer, D.; Lopez-Royo, F. Biophotonic Ring Resonator for Ultrasensitive Detection of DMMP As a Simulant for Organophosphorus Agents. *Anal. Chem.* **2014**, *86*, 5125–5130.
10. Baker, J. E.; Sriram, R.; Miller, B. L. Two-Dimensional Photonic Crystals for Sensitive Microscale Chemical and Biochemical Sensing. *Lab Chip* **2015**, *15*, 971–990.
11. Agranovich, V. M.; Mills, D. L. *Surface Polaritons*; North Holland Publishing Company: Amsterdam, 1982.
12. Slavik, R.; Homola, J.; Vaisocherova, H. Advanced Biosensing using Simultaneous Excitation of Short and Long Range Surface Plasmons. *Meas. Sci. Technol.* **2006**, *17*, 932–938.
13. Homola, J. *Surface Plasmon Resonance based Sensors*; Springer: 2006.
14. Homola, J. Surface Plasmon Resonance Sensors for Detection of Chemical and Biological Species. *Chem. Rev.* **2008**, *108*, 462–493.
15. Dutta-Gupta, S.; Martin, O. J. F. Strongly Coupled Bio-Plasmonic System: Application to Oxygen Sensing. *J. Appl. Phys.* **2011**, *110*, 044701.
16. Kvasnika, P.; Chadt, K.; Vala, M.; Bockova, M.; Homola, J. Toward Single-Molecule Detection with Sensors Based on Propagating Surface Plasmons. *Opt. Lett.* **2012**, *37*, 163–165.
17. Sipova, H.; Vrba, D.; Homola, J. Analytical Value of Detecting an Individual Molecular Binding Event: The Case of the Surface Plasmon Resonance Biosensor. *Anal. Chem.* **2012**, *84*, 30–33.
18. Unger, A.; Kreiter, M. Analyzing the Performance of Plasmonic Resonators for Dielectric Sensing. *J. Phys. Chem. C* **2009**, *113*, 12243–12251.
19. Hao, F.; Sonnefraud, Y.; Dorpe, P. V.; Maier, S. A.; Halas, N. J.; Nordlander, P. Symmetry Breaking in Plasmonic Nanocavities: Subradiant LSPR Sensing and a Tunable Fano Resonance. *Nano Lett.* **2008**, *8*, 3983–3988.
20. Sonnefraud, Y.; Verellen, N.; Sobhani, H.; Vandenbosch, G. A. E.; Moshchalkov, V. V.; Van Dorpe, P.; Nordlander, P.; Maier, S. A. Experimental Realization of Subradiant, Superradiant, and Fano Resonances in Ring/Disk Plasmonic Nanocavities. *ACS Nano* **2010**, *4*, 7.
21. Baciu, C. L.; Becker, J.; Janshoff, A.; Sonnichsen, C. Protein-Membrane Interaction Probed by Single Plasmonic Nanoparticles. *Nano Lett.* **2008**, *8*, 1724–1728.
22. Stewart, M. E.; Anderton, C. R.; Thompson, L. B.; Maria, J.; Gray, S. K.; Rogers, J. A.; Nuzzo, R. G. Nanostructured Plasmonic Sensors. *Chem. Rev.* **2008**, *108*, 494–521.
23. Zhang, J.; Atay, T.; Nurmikko, A. V. Optical Detection of Brain Cell Activity Using Plasmonic Gold Nanoparticles. *Nano Lett.* **2009**, *9*, 519–524.
24. Unger, A.; Rietzler, U.; Berger, R.; Kreiter, M. Sensitivity of Crescent-Shaped Metal Nanoparticles to Attachment of Dielectric Colloids. *Nano Lett.* **2009**, *9*, 2311–2315.
25. Chen, J. I. L.; Chen, Y.; Ginger, D. S. Plasmonic Nanoparticle Dimers for Optical Sensing of DNA in Complex Media. *J. Am. Chem. Soc.* **2010**, *132*, 9600–9601.
26. Kuznetsov, A. I.; Evlyukhin, A. B.; Goncalves, M. R.; Reinhardt, C.; Koroleva, A.; Arnedillo, M. L.; Kiyan, R.; Marti, O.; Chichkov, B. N. Laser Fabrication of Large-Scale Nanoparticle Arrays for Sensing Applications. *ACS Nano* **2011**, *5*, 4843–4849.
27. Lassiter, J. B.; Sobhani, H.; Fan, J. A.; Kundu, J.; Capasso, F.; Nordlander, P.; Halas, N. J. Fano Resonances in Plasmonic Nanoclusters: Geometrical and Chemical Tunability. *Nano Lett.* **2010**, *10*, 3184–3189.
28. Kubo, W.; Fujikawa, S. Au Double Nanopillars with Nanogap for Plasmonic Sensor. *Nano Lett.* **2011**, *11*, 8–15.
29. Zhang, W.; Huang, L.; Santschi, C.; Martin, O. J. F. Trapping and Sensing 10 nm Metal Nanoparticles Using Plasmonic Dipole Antennas. *Nano Lett.* **2010**, *10*, 1006–1011.
30. Nusz, G. J.; Curry, A. C.; Marinakos, S. M.; Wax, A.; Chilkoti, A. Rational Selection of Gold Nanorod Geometry for Label-Free Plasmonic Biosensors. *ACS Nano* **2009**, *3*, 795–806.
31. Bahramipanah, M.; Abrishamian, M. S.; Mirtaheri, S. A.; Liu, J. M. Ultracompact Plasmonic Loop−Stub Notch Filter and Sensor. *Sens. Actuators, B* **2014**, *194*, 311–318.
32. Zhang, W.; Martin, O. J. F. A Universal Law for Plasmon Resonance Shift in Biosensing. *ACS Photonics* **2015**, *2*, 144–150.
33. Mayer, K. M.; Hafner, J. H. Localized Surface Plasmon Resonance Sensors. *Chem. Rev.* **2011**, *111*, 3828–3857.
34. Anker, J. N.; Hall, W. P.; Lyandres, O.; Shah, N. C.; Zhao, J.; Van Duyne, R. P. Biosensing with Plasmonic Nanosensors. *Nat. Mater.* **2008**, *7*, 442–453.
35. Brolo, A. G. Plasmonics for Future Biosensors. *Nat. Photonics* **2012**, *6*, 709–713.
36. Wang, H.; Brandl, D. W.; Le, F.; Nordlander, P.; Halas, N. J. Nanorice: A Hybrid Plasmonic Nanostructure. *Nano Lett.* **2006**, *6*, 827–832.
37. Nehl, C. L.; Liao, H.; Hafner, J. H. Optical Properties of Star-Shaped Gold Nanoparticles. *Nano Lett.* **2006**, *6*, 683–688.
38. Chen, H. J.; Kou, X. S.; Yang, Z.; Ni, W. H.; Wang, J. F. Shape- and Size-Dependent Refractive Index Sensitivity of Gold Nanoparticles. *Langmuir* **2008**, *24*, 5233–5237.
39. Cao, J.; Sun, T.; Grattan, K. T. V. Gold Nanorod-Based Localized Surface Plasmon Resonance Biosensors: A review. *Sens. Actuators, B* **2014**, *195*, 332–351.
40. Estevez, M. C.; Otte, M. A.; Sepulveda, B.; Lechuga, L. M. Trends and Challenges of Refractometric Nanoplasmonic Biosensors: A review. *Anal. Chim. Acta* **2014**, *806*, 55–73.
41. Prasad, J.; Zins, I.; Branscheid, R.; Becker, J.; Koch, A. H. R.; Fytas, G.; Kolb, U.; Sonnichsen, C. Plasmonic Core−Satellite Assemblies as Highly Sensitive Refractive Index Sensors. *J. Phys. Chem. C* **2015**, *119*, 5577–5582.
42. Soler, M.; Mesa-Antunez, P.; Estevez, M. C.; Ruiz-Sanchez, A. J.; Otte, M. A.; Sepulveda, B.; Collado, D.; Mayorga, C.; Torres, M. J.; Perez-Inestrosa, E.; et al. Highly Sensitive Dendrimer-Based Nanoplasmonic Biosensor for Drug Allergy Diagnosis. *Biosens. Bioelectron.* **2015**, *66*, 115–123.
43. Lee, K.-S.; El-Sayed, M. A. Gold and Silver Nanoparticles in Sensing and Imaging: Sensitivity of Plasmon Response to Size, Shape, and Metal Composition. *J. Phys. Chem. B* **2006**, *110*, 19220–19225.
44. Willets, K. A.; Van Duyne, R. P. Localized Surface Plasmon Resonance Spectroscopy and Sensing. *Annu. Rev. Phys. Chem.* **2007**, *58*, 267–297.
45. Abasahl, B.; Dutta-Gupta, S.; Santschi, C.; Martin, O. J. F. Coupling Strength Can Control the Polarization Twist of a Plasmonic Antenna. *Nano Lett.* **2013**, *13*, 4575–4579.
46. Prodan, E.; Radloff, C.; Halas, N. J.; Nordlander, P. A Hybridization Model for the Plasmon Response of Complex Nanostructures. *Science* **2003**, *302*, 419–422.
47. Aubry, A.; Lei, D. Y.; Maier, S. A.; Pendry, J. B. Interaction between Plasmonic Nanoparticles Revisited with Transformation Optics. *Phys. Rev. Lett.* **2010**, *105*, 233901.
48. Rahmani, M.; Lei, D. Y.; Giannini, V.; Lukiyanchuk, B.; Ranjbar, M.; Liew, T. Y. F.; Hong, M.; Maier, S. A. Subgroup Decomposition of Plasmonic Resonances in Hybrid Oligomers: Modeling the Resonance Lineshape. *Nano Lett.* **2012**, *12*, 2101–2106.
49. Bolduc, O. R.; Live, L. S.; Masson, J. F. High-Resolution Surface Plasmon Resonance Sensors based on a Dove Prism. *Talanta* **2009**, *77*, 1680–1687.

50. Lee, D. E.; Lee, T.-W.; Kwon, S.-H. Spatial Mapping of Refractive Index based on a Plasmonic Tapered Channel Waveguide. *Opt. Express* **2015**, *23*, 5907–5914.
51. Christ, A.; Ekinci, Y.; Solak, H. H.; Gippius, N. A.; Tikhodeev, S. G.; Martin, O. J. F. Controlling the Fano Interference in a Plasmonic Lattice. *Phys. Rev. B: Condens. Matter Mater. Phys.* **2007**, *76*, 201405.
52. Liu, N.; Langguth, L.; Weiss, T.; Kastel, J.; Fleischhauer, M.; Pfau, T.; Giessen, H. Plasmonic Analogue of Electromagnetically Induced Transparency at the Drude Damping Limit. *Nat. Mater.* **2009**, *8*, 758–762.
53. Gallinet, B.; Martin, O. J. F. Influence of Electromagnetic Interactions on the Line Shape of Plasmonic Fano Resonances. *ACS Nano* **2011**, *5*, 8999–9008.
54. Gallinet, B.; Martin, O. J. F. Relation between Nearfield and Farfield Properties of Plasmonic Fano Resonances. *Opt. Express* **2011**, *19*, 22167–22175.
55. Gallinet, B.; Martin, O. J. F. Ab Initio Theory of Fano Resonances in Plasmonic Nanostructures and Metamaterials. *Phys. Rev. B: Condens. Matter Mater. Phys.* **2011**, *83*, 235427.
56. Gallinet, B.; Martin, O. J. F. Refractive Index Sensing with Subradiant Modes: A Framework To Reduce Losses in Plasmonic Nanostructures. *ACS Nano* **2013**, *7*, 6978–6987.
57. Lovera, A.; Gallinet, B.; Nordlander, P.; Martin, O. J. F. Mechanisms of Fano Resonances in Coupled Plasmonic Systems. *ACS Nano* **2013**, *7*, 4527–4536.
58. Yan, C.; Martin, O. J. F. Periodicity-Induced Symmetry Breaking in a Fano Lattice: Hybridization and Tight-Binding Regimes. *ACS Nano* **2014**, *8*, 11860–11868.
59. Leveque, G.; Martin, O. J. F. Tunable Composite Nanoparticle for Plasmonics. *Opt. Lett.* **2006**, *31*, 2750–2752.
60. Farhang, A.; Ramakrishna, S. A.; Martin, O. J. F. Compound Resonance-Induced Coupling Effects in Composite Plasmonic Metamaterials. *Opt. Express* **2012**, *20*, 29447–29456.
61. Farhang, A.; Bigler, N.; Martin, O. J. F. Coupling of Multiple LSP and SPP Resonances: Interactions between an Elongated Nanoparticle and a Thin Metallic Film. *Opt. Lett.* **2013**, *38*, 4758–4761.
62. Farhang, A.; Siegfried, T.; Ekinci, Y.; Sigg, H.; Martin, O. J. F. Large-Scale Sub-100 nm Compound Plasmonic Grating Arrays to Control the Interaction Between Localized and Propagating Plasmons. *J. Nanophotonics* **2014**, *8*, 083897.
63. Artar, A.; Yanik, A. A.; Altug, H. Fabry–Perot Nanocavities in Multilayered Plasmonic Crystals for Enhanced Biosensing. *Appl. Phys. Lett.* **2009**, *95*, 051105.
64. Ameling, R.; Langguth, L.; Hentschel, M.; Mesch, M.; Braun, P. V.; Giessen, H. Cavity-Enhanced Localized Plasmon Resonance Sensing. *Appl. Phys. Lett.* **2010**, *97*, 253116.
65. Chanda, D.; Shigeta, K.; Truong, T.; Lui, E.; Mihi, A.; Schulmerich, M.; Braun, P. V.; Bhargava, R.; Rogers, J. A. Coupling of Plasmonic and Optical Cavity Modes in Quasi-Three-Dimensional Plasmonic Crystals. *Nat. Commun.* **2011**, *2*, 479.
66. Xu, J.; Guan, P.; Kvasnička, P.; Gong, H.; Homola, J.; Yu, Q. Light Transmission and Surface-Enhanced Raman Scattering of Quasi-3D Plasmonic Nanostructure Arrays with Deep and Shallow Fabry-Perot Nanocavities. *J. Phys. Chem. C* **2011**, *115*, 10996–11002.
67. Saison-Francioso, O.; Leveque, G.; Akjouj, A.; Pennec, Y.; Djafari-Rouhani, B.; Szunerits, S.; Boukherroub, R. Plasmonic Nanoparticles Array for High-Sensitivity Sensing: A Theoretical Investigation. *J. Phys. Chem. C* **2012**, *116*, 17819–17827.
68. Schmidt, M. A.; Lei, D. Y.; Wondraczek, L.; Nazabal, V.; Maier, S. A. Hybrid Nanoparticle–Microcavity-Based Plasmonic Nanosensors with Improved Detection Resolution and Extended Remote-Sensing Ability. *Nat. Commun.* **2012**, *3*, 1108.
69. Melamud, R.; Davenport, A. A.; Hill, G. C.; Chan, I. H.; Declercq, F.; Hartwell, P. G.; Pruitt, B. L. In Development of an SU-8 Fabry-Perot Blood Pressure Sensor. *IEEE Int. Conf. MEMS* **2005**, 810–813.
70. Yan, Z.; Xiaopei, C.; Yongxin, W.; Cooper, K. L.; Anbo, W. Microgap Multicavity Fabry Perot Biosensor. *J. Lightwave Technol.* **2007**, *25*, 1797–1804.
71. St-Gelais, R.; Masson, J.; Peter, Y.-A. All-Silicon Integrated Fabry–Perot Cavity for Volume Refractive Index Measurement in Microfluidic Systems. *Appl. Phys. Lett.* **2009**, *94*, 243905.
72. Lu, G.; Hupp, J. T. Metal–Organic Frameworks as Sensors: A ZIF-8 Based Fabry–Perot Device as a Selective Sensor for Chemical Vapors and Gases. *J. Am. Chem. Soc.* **2010**, *132*, 7832–7833.
73. Li Han, C.; Xiu Min, A.; Chi Chiu, C.; Shaillender, M.; Neu, B.; Wei Chang, W.; Peng, Z.; Kam Chew, L. Layer-By-Layer (Chitosan/Polystyrene Sulfonate) Membrane-Based Fabry-Perot Interferometric Fiber Optic Biosensor. *IEEE J. Sel. Top. Quantum Electron.* **2012**, *18*, 1457–1464.
74. Wu, H.; Huang, H.; Bai, M.; Liu, P.; Chao, M.; Hu, J.; Hao, J.; Cao, T. An Ultra-Low Detection-Limit Optofluidic Biosensor Based on All Glass Fabry-Perot Cavity. *Opt. Express* **2014**, *22*, 31977–31983.
75. Pengbo, L.; Hui, H.; Tun, C.; Min, B.; Haibo, W.; Xueyu, L.; Zhenan, T. An Ultra-Low Detection-Limit Optofluidic Biosensor Based on Fabry-Perot Cavity. *IEEE Int. Conf. Control Autom.* **2014**, 1264–1268.
76. Yuan, G.; Gao, L.; Chen, Y.; Wang, J.; Ren, P.; Wang, Z. Efficient Optical Biochemical Sensor with Slotted Bragg-Grating-Based Fabry–Perot Resonator Structure in Silicon-on-Insulator Platform. *Opt. Quantum Electron.* **2015**, *47*, 247–255.
77. Subimal, D.; Shourya Dutta, G.; Banerji, J.; Gupta, S. D. Critical Coupling at Oblique Incidence. *J. Opt. A: Pure Appl. Opt.* **2007**, *9*, 555.
78. Langhammer, C.; Schwind, M.; Kasemo, B.; Zoric, I. Localized Surface Plasmon Resonances in Aluminum Nanodisks. *Nano Lett.* **2008**, *8*, 1461–1471.
79. Ciftlik, A. T.; Gijs, M. A. M. A Low-Temperature Parylene-to-Silicon Dioxide Bonding Technique for High-Pressure Microfluidics. *J. Micromech. Microeng.* **2011**, *21*, 035011.
80. Auzelyte, V.; Gallinet, B.; Flauraud, V.; Santschi, C.; Dutta-Gupta, S.; Martin, O. J. F.; Brugger, J. Large-Area Gold/Parylene Plasmonic Nanostructures Fabricated by Direct Nanocutting. *Adv. Opt. Mater.* **2013**, *1*, 50–54.
81. Piotter, V.; Hanemann, T.; Ruprecht, R.; Haußelt, J. Injection Molding and Related Techniques for Fabrication of Microstructures. *Microsyst. Technol.* **1997**, *3*, 129–133.
82. Sacks, O. *CRC Handbook of Chemistry and Physics*; CRC Press: 2004.
83. Fischer, H.; Martin, O. J. F. Engineering the Optical Response of Plasmonic Nanoantennas. *Opt. Express* **2008**, *16*, 9144–9154.